INORGANIC CHEMISTRY FRONTIERS

RESEARCH ARTICLE

View Article Online
View Journal | View Issue

Cite this: *Inorg. Chem. Front.*, 2023, **10**, 3273

A new 0D–2D $CsPbBr_3$–Co_3O_4 heterostructure photocatalyst with efficient charge separation for photocatalytic CO_2 reduction†

Xin Zhong,‡[a] Xinmeng Liang,‡[a] Xinyu Lin,[a] Jin Wang, *[a,b] Malik Zeeshan Shahid *[a] and Zhengquan Li *[a,b]

The effective spatial separation of photogenerated charge carriers is essential for realizing efficient CO_2 conversion. Herein, a new $CsPbBr_3$–Co_3O_4 heterostructure photocatalyst was rationally developed for photocatalytic CO_2 reduction. A facile synthetic strategy based on electrostatic interactions was utilized. The results revealed that the $CsPbBr_3$–Co_3O_4 hybrid exhibited a boosted evolution rate of 64.6 μmol g^{-1} h^{-1} (CO: 35.40 μmol g^{-1} h^{-1}; CH_4: 29.2 μmol g^{-1} h^{-1}) with an electron consumption rate ($R_{electron}$) of 304.4 μmol g^{-1} h^{-1}, surpassing pristine $CsPbBr_3$ or Co_3O_4. The high activity mainly arises from efficient charge separation and the directional transfer of electrons from $CsPbBr_3$ to Co_3O_4 *via* an intimately coupled heterointerface. Notably, the surface features (derived from the unique morphology) expedited the CO_2 adsorption and accumulation of electrons at the Co_3O_4 site which ultimately facilitated the conversion of CO_2 over the $CsPbBr_3$–Co_3O_4 composite. This approach provides a strategy to design and modulate highly active metal oxide and perovskite-based photocatalysts and presents great potential for constructing a heterointerface for CO_2 reduction.

Received 21st March 2023,
Accepted 17th April 2023

DOI: 10.1039/d3qi00527e

rsc.li/frontiers-inorganic

1. Introduction

The daily consumption of fossil fuels results in the emission of CO_2, causing universal environmental and energy issues.[1–4] Fixation of CO_2 into value-added products such as CO, CH_4, HCOOH, CH_3OH, *etc.* *via* solar-driven catalysis, also known as artificial photosynthesis, is a clean and sustainable solution.[5–7] However, it is challenging and suffers low conversion efficiency due to the high thermodynamic stability of CO_2 molecules and the need for multi-electron transfer.[8,9] Recently, instead of using single-component photocatalysts, research efforts have been diverted to designing their low-cost heterostructures. Many materials, such as C_3N_4,[10,11] ZrO_2,[12] TiO_2,[13] Ta_2O_5,[14] Nb_2O_5,[15] metal sulfides,[16] metal–organic frameworks,[17] metal complexes,[7] single-atom catalysts,[18] MXenes,[19] conducting polymers,[20] metal halide perovskites,[6,21] *etc.*, have been reported aiming at activity enhancement *via* optimizing the light-harvesting and charge carrier kinetics. However, the search for a more effective candidate photocatalyst has not stopped.

Among numerous materials, all inorganic metal halide perovskites, particularly cesium lead-bromide perovskite quantum dots ($CsPbBr_3$ QDs), are extremely competitive photocatalysts for CO_2 reduction.[1,6,22,23] This is owing to their suitable energy band structure, small size, defect tolerance, and large carrier mobility as compared to other inorganic metal halide family members, *e.g.* $CsPbCl_3$ and $CsPbI_3$.[1,6,24–43] However, pristine $CsPbBr_3$ QDs suffer from instability and rapid recombination of electron–hole (e^-–h^+) pairs, leading to low activity. To address this issue, Xu *et al.* first utilized the $CsPbBr_3$ QDs/graphene composite for the photocatalytic reduction of CO_2.[43] After that, several efforts were devoted to enhance its performance. For instance, our group designed $CsPbBr_3$ QDs/Bi_2WO_6[38] and $CsPbBr_3$ QDs coupled with covalent triazine frameworks,[36] and both exhibited enhanced charge separation and led to improved CO_2 photoreduction. But the produced gas was mainly CO and only a minimum of CH_4 was detected. This was possibly due to the lack of sufficient accumulation of reductive electrons at catalytic sites.

[a]*Key Laboratory of the Ministry of Education for Advanced Catalysis Materials, Zhejiang Normal University, Jinhua, Zhejiang 321004, P. R. China. E-mail: zqli@zjnu.edu.cn, zeeshan-nano@zjnu.edu.cn, wangjin@zjnu.edu.cn*
[b]*Zhejiang Institute of Optoelectronics, Zhejiang Normal University, Jinhua, Zhejiang 321004, P. R. China*

†Electronic supplementary information (ESI) available. See DOI: https://doi.org/10.1039/d3qi00527e

‡These authors contributed equally.

So, we further our research to find some suitable materials which can form an intimately coupled interface with $CsPbBr_3$ QDs and enable efficient photocatalysis to generate both CO and CH_4, thereby overcoming the intrinsic issues of $CsPbBr_3$ QDs.

We found that the transition metal oxide photocatalyst cobalt oxide (Co_3O_4) is an ideal non-precious catalyst for CO_2 reduction as it exhibits suitable band alignment, efficient charge-carrier flux capability, and chemical/thermodynamic stability.[44–52] However, the typical single component Co_3O_4 may suffer limited preservation of reductive electrons as well as hindered spatial separation of e^-–h^+ pairs. Multiple morphologies have been constructed to meet such limitations, such as nanorods,[53] ultrathin nanosheets,[54] nanofibers,[55] hollow dodecahedra,[48] porous structures,[56] and mesoporous two-dimensional (2D) hexagonal nanoplatelets (HPs) with various facets and catalytically active sites.[45,57] For example, Gao *et al.* first developed [112] facet-rich Co_3O_4 HPs,[52] and then later on Zhu *et al.* constructed the Co_3O_4/g-C_3N_4 (2D/2D) hybrid,[57] both intended to facilitate the separation of charge carriers for photocatalytic CO_2 conversion. Inspiringly, we intend to develop a high-performance Co_3O_4 heterostructure catalyst by simultaneously promoting charge separation and preserving the reductive electrons. It is widely accepted that constructing a heterostructure is efficient for channelizing and accelerating the separation and transfer of e^-–h^+ pairs *via* a strongly coupled interface developed through proper band alignment and work functions (Φ).[47,58–61] Therefore, constructing a hybrid between $CsPbBr_3$ QDs and CO_3O_4 HPs probably can result in an improved photocatalytic performance toward CO_2 reduction. To the best of our knowledge, there is no report on the fabrication of $CsPbBr_3$ QDs on CO_3O_4 HPs, and it is desirable to design and construct a new heterostructure based on $CsPbBr_3$ QDs and CO_3O_4 HPs for CO_2 photoreduction.

Herein, a $CsPbBr_3$–Co_3O_4 heterojunction photocatalyst is developed *via* electrostatic self-assembly between CO_3O_4 HPs and $CsPbBr_3$ QDs for photocatalytic CO_2 reduction. Investigations confirmed the successful formation of the $CsPbBr_3$–Co_3O_4 hybrid. Diverse physicochemical and optoelectronic characterization studies revealed that: (i) CO_3O_4 HPs acted as a supporting matrix to collect electrons from $CsPbBr_3$, rendering electron localization; (ii) the $CsPbBr_3$–Co_3O_4 hybrid exhibited compact heterointerfaces, facilitating robust charge separation with hampered e^-–h^+ pair recombination; (iii) the Co_3O_4 side offers numerous mesopores and catalytic sites, which facilitate the better capturing and activation of CO_2 molecules. Consequently, $CsPbBr_3$–Co_3O_4 showed improved activity for the generation of CO and CH_4, with an evolving rate of 35.40 and 29.2 μmol g^{-1} h^{-1}, respectively, surpassing their pristine counterparts *i.e.*, $CsPbBr_3$ QDs and CO_3O_4 HPs, as well as recent state-of-the-art photocatalysts (Table S1†). This work highlights the rational design of new metal halide perovskite-based photocatalysts and addresses the critical issues regarding charge carrier kinetics to realize efficient solar-driven CO_2 conversion.

2. Experimental section

2.1. Synthesis of $CsPbBr_3$ QDs

To obtain $CsPbBr_3$ QDs, the reported method was followed (see also in Fig. S1†).[62] Briefly, for the Cs-OA stock solution, 0.2 g of cesium carbonate (Cs_2CO_3), 10 mL of octadecene (ODE, $C_{18}H_{36}$), and 0.6 mL of oleic acid (OA, $C_{18}H_{34}O_2$) were loaded into a three-necked round bottom flask. Under Ar flow, the temperature was increased to 120 °C and a clear light-yellow solution was obtained. The temperature was increased to 150 °C just before the hot injection. For the Pb stock solution, 0.1380 g of lead bromide ($PbBr_2$) and 10 mL of ODE were added into a 50 mL three-necked round bottom flask, under Ar flow, the temperature was increased to 120 °C to get a white turbid liquid and maintained it for 30 min. Next, the temperature was further increased to 165 °C, and 1.5 mL OA and 1.1 mL OAm were added to the Pb stocks. When a yellow homogeneous solution was obtained, 0.8 mL of the Cs-stock solution was swiftly injected into it. After 5 s, the mixture was immediately cooled down using an ice-water bath. The original solution was directly centrifuged at 8000 rpm for 5 min and further washed with ethyl acetate and isopropanol to remove the organic residue. Finally, the $CsPbBr_3$ QDs collected and stored in *n*-hexane are added in an equal volume.

2.2. Preparation of Co_3O_4 HPs

To obtain Co_3O_4 HPs, the previously reported method was modified (see also in Fig. S2†).[52] Firstly, β-$Co(OH)_2$ precipitates were prepared. 0.2379 g (5 mmol) of cobalt chloride hexahydrate ($CoCl_2·6H_2O$), 1.6823 g (60 mmol) of cyclohexamethylenetetramine (urotropine), 180 mL of deionized water and 20 mL of ethanol were added into a beaker under stirring. The mixture was heated in an oil bath to 90 °C for 1 h to obtain a pink solution. After cooling it to an ambient temperature, it was centrifuged at 9000 rpm for 15 min to obtain a pink precipitate of β-$Co(OH)_2$. Subsequently, 50 mL of deionized water and 50 mL of ethanol were added, and the β-$Co(OH)_2$ precipitate was redispersed by ultrasonication. The sample was collected by centrifuging at 9000 rpm for 15 min. This operation was repeated 3 times. The obtained precipitate was freeze-dried under vacuum for 6 hours. Finally, the precipitate was transferred into a cuboid crucible and put into a muffle furnace for calcination at 400 °C for 3 h to obtain a black powder of Co_3O_4 HPs.

2.3. Synthesis of the $CsPbBr_3$–Co_3O_4 heterostructure

The $CsPbBr_3$–Co_3O_4 heterostructure was prepared using a solution-processed approach at room temperature. First, 0.5 mg of the Co_3O_4 HP powder was dispersed into 250 μL of ethanol under uninterrupted stirring. Second, 400 μL (2 mg) of $CsPbBr_3$ QDs were dispersed into 5 mL of ethyl acetate. Third, the $CsPbBr_3$ QD solution was swiftly added into the solution of Co_3O_4 HPs and mechanically stirred at room temperature in the dark for 30 min. Finally, the mixture was ultrasonicated for another 30 min under ambient conditions. The obtained solution was centrifuged at 8000 rpm for 5 min, and the precipitate was vacuum dried overnight at 45 °C to obtain the $CsPbBr_3$–Co_3O_4 heterojunction. This synthesis was performed with an optimum mass ratio (Co_3O_4 HPs : $CsPbBr_3$ QDs) *i.e.*, 1 : 4, and a similar method was followed to obtain various mass ratios such as 1 : 1, 1 : 2, 1 : 8, and 1 : 16. Step by step addition of Co_3O_4 HPs and $CsPbBr_3$ QDs as well as the formation process of the $CsPbBr_3$–Co_3O_4 heterojunction are also picturized and described in Fig. S3.† The details of all materials and other characterization studies for physicochemical and opto-electronic properties are provided in the ESI.†

3. Results and discussion

3.1. Illustration of the synthesis process and verification of the heterostructure formation

Firstly, $CsPbBr_3$ QDs (0D) was precisely prepared *via* a typical hot-injection method (Fig. S1†).[62] Subsequently, Co_3O_4 HPs (2D) holding rich facets [112] were synthesized through the calcination of brucite-like cobalt hydroxide β-$Co(OH)_2$ precipitates (Fig. S2†).[52] Finally, to obtain a 0D/2D $CsPbBr_3$–Co_3O_4 heterojunction, their mixture at an optimum mass ratio 4 : 1 ($CsPbBr_3$ QDs : Co_3O_4 HPs) was exclusively stirred in a solution of ethyl acetate and ethanol at room temperature (Scheme 1, see details in Fig. S3†). The tactic used here is based on the Coulomb electrostatic assembly which enables the incorporation of $CsPbBr_3$ QDs and Co_3O_4 HPs. The zeta potentials of pristine $CsPbBr_3$ QDs and Co_3O_4 HPs are 4.80 mV and −3.10 mV, respectively (Fig. S4†), which indicates oppositely charged surfaces encounter electrostatic attractions, resulting in the formation of $CsPbBr_3$–Co_3O_4. Such a kind of electrostatic self-assembly would possess a strong heterointerface, beneficial for interfacial charge transfer.[63]

To confirm the successful formation of the $CsPbBr_3$–Co_3O_4 hybrid, powder X-ray diffraction (XRD) was first conducted (Fig. 1a). Pristine $CsPbBr_3$ QDs exhibit a typical cubic-phase (JCPDS card, No. 75-0412). Meanwhile, pristine Co_3O_4 HPs show diffraction patterns associated with the face-centred cubic phase of the spinel Co_3O_4 (JCPDS card No. 74-1657). Notably, strong signals of all peaks emerged and co-existed in the $CsPbBr_3$–Co_3O_4 hybrid, illustrating the successful formation of the heterojunction and the crystal phases were well maintained. To confirm this claim, nitrogen adsorption–desorption analysis was performed (Table S2†). It can be seen that after the precise formation of the heterojunction, the pore size and pore volume were reduced from 31.3 nm to 21.21 nm

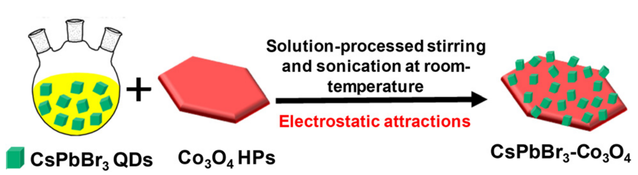

Scheme 1 Illustration for the formation of the $CsPbBr_3$–Co_3O_4 heterojunction *via* electrostatic attraction.

and 0.1325 $cm^3\ g^{-1}$ to 0.0266 $cm^3\ g^{-1}$ respectively. In addition, the BET surface area also decreased from 16.9 $m^2\ g^{-1}$ to 5.016 $m^2\ g^{-1}$. This result indicates that the mesopores of Co_3O_4 were occupied by $CsPbBr_3$ QDs. Besides in the XRD, an exclusive color transformation was observed from black (Co_3O_4-HPs, Fig. 1b) and bright yellow ($CsPbBr_3$ QDs, Fig. 1c) to dark grey ($CsPbBr_3$–Co_3O_4, Fig. 1d). In addition, under ultraviolet irradiation, the $CsPbBr_3$–Co_3O_4 heterojunction demonstrated a dark green fluorescence in comparison with the bright green fluorescence of $CsPbBr_3$ QDs (Fig. S5†). Such color transformations further endorse that the heterojunction was constructed successfully in a well-controlled manner *via* a current facile strategy.

Transmission electron microscopy (TEM) and scanning electron microscopy (SEM) analysis further confirmed the formation of the heterojunction. $CsPbBr_3$ QDs exhibited an average size of about 12 nm (Fig. 1e and inset), whereas Co_3O_4 exhibits a hexagonal platelet-like structure with lateral sizes of ∼4 ± 1 μm, and a thickness of about ∼50 ± 10 nm, a dominant facet (112), and mesopores (Fig. 1f and inset). Importantly, after incorporating $CsPbBr_3$ QDs into Co_3O_4 HPs, several facts were noticed. (i) Both $CsPbBr_3$ QDs and Co_3O_4 HPs co-existed with well-defined morphologies, and their sizes were preserved without any further ripening, verifying that the synthesis was well-controlled (Fig. 1g). (ii) Besides electrostatic interactions, the huge surface energy of $CsPbBr_3$ QDs could drive its face-to-face attaching to Co_3O_4 HPs. (iii) $CsPbBr_3$ QDs were well dispersed (denoted by yellow circles) all over Co_3O_4 HPs, both on the inner side (Fig. 1g and inset) and on the boundary sides (Fig. 1h) and this would facilitate the formation of a rich heterointerface. (iv) Even though most of the mesopores were occupied by $CsPbBr_3$ QDs, still many mesopores could be observed as denoted by the marked area in green (Fig. 1g, h, and the inset).

Such accessible mesopores are not only beneficial for supporting CO_2 adsorption but also facilitate the exposure of the innermost lattice surfaces for the rapid transfer of photo-induced e^- to the outermost active surface sites.[52,57] More clear evidence regarding the formation of the heterointerface was collected *via* high-resolution TEM analysis (HRTEM, Fig. 1i and j). The spacing in the lattice fringes was found to match well with both constituents, that is, 0.58 nm and 0.285 nm being the corresponding planes of $CsPbBr_3$ and Co_3O_4 respectively (Fig. 1j). Accordingly, the HAADF and energy dispersive X-ray (EDX) mapping analysis depicts the precise incorporation and distribution of all elements including Cs, Pb, Br, Co, and O in the $CsPbBr_3$–Co_3O_4 heterojunction (Fig. 1k–p). The above results are in-line with the XRD and TEM analysis, validating the formation of the heterojunction with finely dispersed $CsPbBr_3$ QDs on the support matrix of Co_3O_4 HPs.

Next, surface chemical states and interfacial interaction in the $CsPbBr_3$–Co_3O_4 heterojunction were evaluated *via* high-resolution X-ray photoelectron spectroscopy (XPS) of Cs 3d, Pb 4f, Br 3d, Co 2p, and O 1s. It is noteworthy that, in comparison with $CsPbBr_3$ QDs, the binding energy of Cs 3d (Fig. 2a), Pb 4f

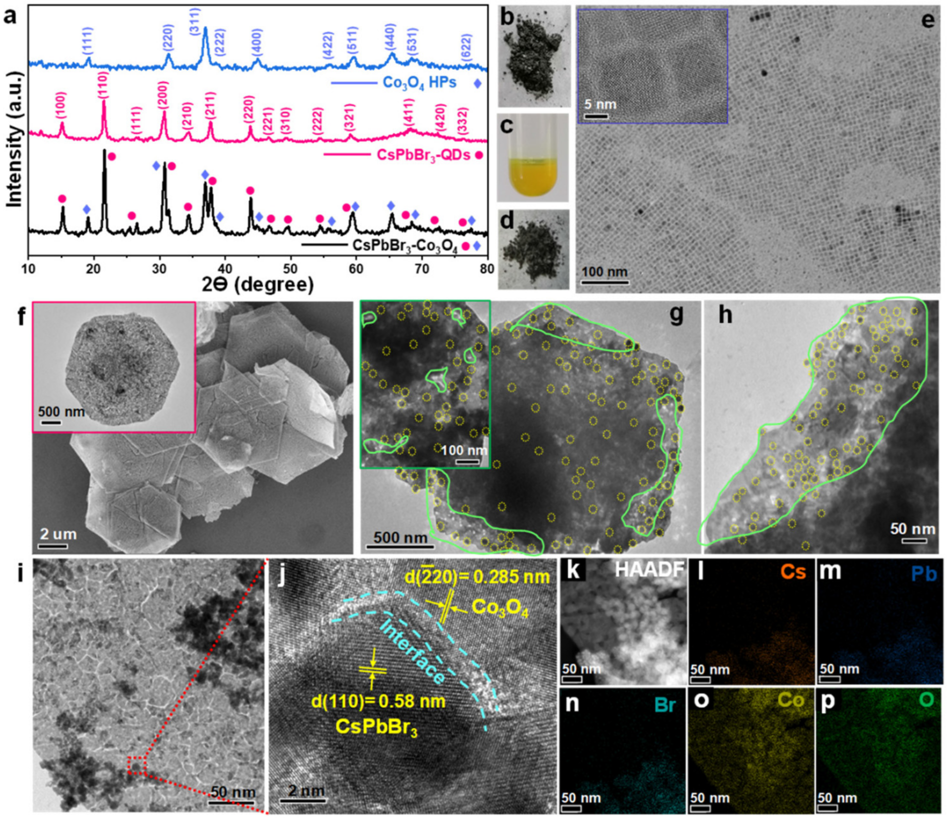

Fig. 1 (a) Comparison of the XRD pattern for the as-prepared products within the 2 theta range 10°–80°, where pink circles and blue diamonds denote the corresponding peaks in the Co_3O_4–$CsPbBr_3$ heterojunction originating from pristine products. Exclusive color transformation of the as-synthesized products where (b) Co_3O_4 HPs black, (c) $CsPbBr_3$ QDs bright yellow, and (d) $CsPbBr_3$–Co_3O_4 dark grey. (e) The TEM image of pristine $CsPbBr_3$ QDs and the corresponding inset with high magnification. (f) The SEM image with low magnification and the inset is the TEM image for a single particle of Co_3O_4 HPs showing a hexagonal platelet-like morphology. (g) The TEM image of a Co_3O_4–$CsPbBr_3$ heterojunction and the corresponding inset which was captured from the central side of a random particle and (h) the image taken from the boundary side. Finely dispersed $CsPbBr_3$ QDs are denoted with yellow circles and the pores are denoted with green marked areas. (i) and (j) HRTEM images, and (k–p) HAADF and EDX mapping results for the Co_3O_4–$CsPbBr_3$ heterojunction.

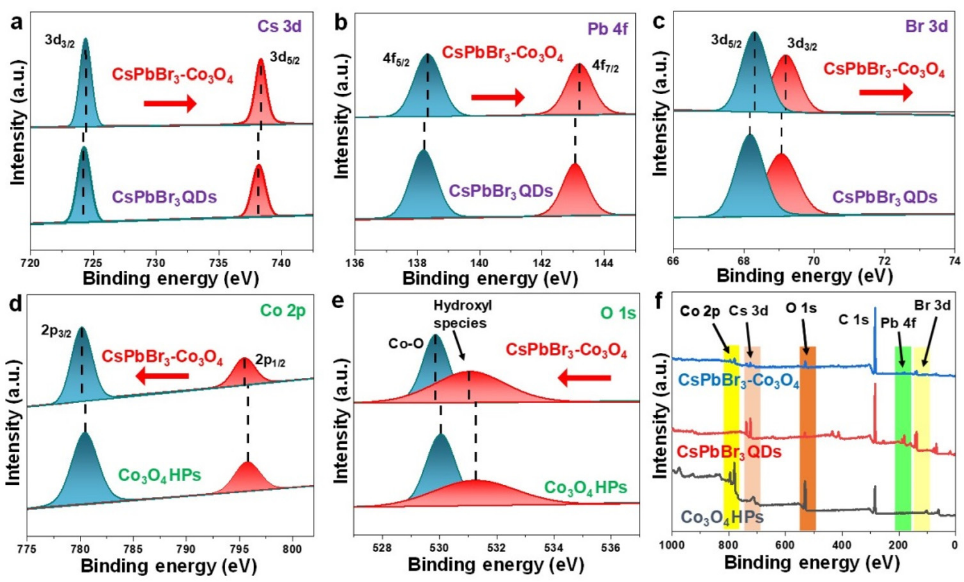

Fig. 2 Comparative representation of high-resolution XPS spectra for (a) Cs 3d, (b) Pb 4f, (c) Br 3d, (d) Co 2p, and (e) O 1s in all the synthesized products. (f) The XPS survey spectrum highlights the co-existence of $CsPbBr_3$ QDs and Co_3O_4 HPs in the $CsPbBr_3$–Co_3O_4 heterojunction.

(Fig. 2b), and Br 3d (Fig. 2c) faced a positive shift in the heterojunction. This result strongly endorsed the close interfacial contact between QDs and HPs. Meanwhile, the XPS of Co 2p spectra signals were comparatively examined for $CsPbBr_3$–Co_3O_4 and Co_3O_4 HPs (Fig. 2d), where two binding energy values at 796 ± 0.2 eV and 780 ± 0.2 eV fit to Co $2p_{1/2}$ and Co $2p_{3/2}$, respectively, which normally attributed to two main regions *i.e.*, Co^{2+} and Co^{3+}.[44] As is known the theoretical value for the atomic ratio Co^{2+}/Co^{3+} is 0.5 (*i.e.*, perfect Co_3O_4), but this value may increase in the presence of surface defects or oxygen vacancies (OVs).[44] Herein, no signal corresponding to defects in O 1s spectra (Fig. 2e) was found, which means that Co_3O_4 synthesized here is perfect and in an equally balanced state. Notably, the absence of OVs also indicates that the high crystallinity of Co_3O_4 was maintained after forming the $CsPbBr_3$–Co_3O_4 heterojunction. Meanwhile, a slight negative shift towards the lower binding energy was observed, demonstrating the interaction between Co_3O_4 and $CsPbBr_3$ (Fig. 2d). Moreover, relative O 1s spectra disclosed two main peaks that fit with the hydroxyl species and Co–O bond respectively. In addition, the obvious co-existence of $CsPbBr_3$ QDs and Co_3O_4 HPs is supported through the XPS survey spectrum (Fig. 2f). All the characteristic peaks are assigned to Cs, Pb, Br, Co, and O (highlighted with bars), affirming the formation of the $CsPbBr_3$–Co_3O_4 heterojunction.

3.2. Investigation of the photocatalytic activity for CO_2 reduction

The activity of the as-synthesized $CsPbBr_3$–Co_3O_4 heterojunction for CO_2 photocatalytic reduction is evaluated under the solid–gas environment using 50 μL of water as the proton source (see details in the ESI section 1.3†).[36,38,63] In particular, no sacrificial agent was used, and visible light was irradiated during photocatalysis. As shown in Fig. 3a, the pristine components only can produce limited CO and negligible CH_4, calculated to be 14.23 and 0.39 (for $CsPbBr_3$ QDs) and 9.52 and 0.46 (for Co_3O_4 HPs) μmol g^{-1} h^{-1}, respectively. Notably, the $CsPbBr_3$–Co_3O_4 heterojunction delivered an enhanced performance for the evolution of CO and CH_4, which is 35.40 and 29.2 μmol g^{-1} h^{-1}, respectively. The corresponding electron consumption rate (R_{electron}, see the formula in Table S2†) was found to be 304.4 μmol g^{-1} h^{-1}, which is 9.51 and 13.4 fold larger than that of pristine $CsPbBr_3$ QDs and Co_3O_4 HPs, respectively. The maximum cumulative production of CO and CH_4 after a 6-hour reaction was 211.58 and 175.31 μmol g^{-1}, respectively (Fig. S6†). The current performance of the $CsPbBr_3$–Co_3O_4 heterojunction was found to be exceeding that of the pristine counter components as well as recent state-of-the-art photocatalysts (Table S1†). Moreover, altering the dosage ratio of $Co_3O_4:CsPbBr_3$ in the heterojunction could greatly influence the activity, for instance, the upper limit of gases was only reached with an optimum mass ratio of 1 : 4 (Fig. S7†).

More and/or less dosage of $CsPbBr_3$ than the optimum value in the heterojunction is not conducive to producing CO and CH_4 in high yields, maybe due to the insufficient amount and/or blockage of active sites respectively, and this phenomenon was found to be consistent with the literature.[38] Additionally, control experiments were performed to confirm the origin of CO, and CH_4 during photocatalysis (Fig. 3b). First, under an argon atmosphere, traces of CO or CH_4 was found, which shows that feed-stock CO_2 is necessary to run the photocatalytic reduction reaction.[36,38,63] Second, nothing was detected under the dark conditions, which again confirms light irradiation is required to obtain CO and CH_4 from the reduction of CO_2. Finally, the optimum result could only be achieved using the $CsPbBr_3$–Co_3O_4 heterojunction with a mass ratio of 1 : 4 as the photocatalyst, CO_2 gas as the feedstock, and solar light illumination (λ > 400 nm). To further verify the origin of the carbon source of the photo-generated CO and CH_4, $^{13}CO_2$ isotope labelling was performed and the GC-MS result is displayed in Fig. S8.† Evidently, the signals belonging to ^{13}CO (*m*/*z* 29) and $^{13}CH_4$ (*m*/*z* 17) are derived from $^{13}CO_2$, validating that CO_2 feedstock is the actual carbon source. Likewise, the oxidation of water to oxygen further validates the continuous supply of protons during CO_2 conversion (Fig. S9†). Furthermore, the $CsPbBr_3$–Co_3O_4 heterojunction can remain stable during the consecutive 5 cycles (Fig. 3c). The morphological and structural characteristics of the $CsPbBr_3$–Co_3O_4 heterojunction are well-maintained after photocatalysis (Fig. S10a and S10b†).

3.3. Unveiling of the origins for improved activity

The origins of the possible enhanced activity were investigated and have been described systematically. The CO_2 adsorption

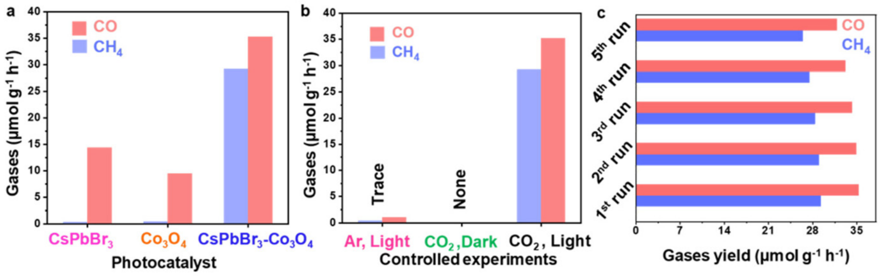

Fig. 3 (a) A comparative depiction of the catalytic activity in terms of the produced gases CO and CH_4 using the as-synthesized $CsPbBr_3$ QDs, Co_3O_4 HPs, and $CsPbBr_3$–Co_3O_4 heterojunction. (b) Controlled experiments were performed under different reaction conditions to produce CO and CH_4 to examine the origin of the evolved gases. (c) Stability test of the $CsPbBr_3$–Co_3O_4 heterojunction for 5 consecutive cycles.

on the surface of the photocatalyst is a primary step that would further govern its activation and conversion. And it is well-known that $CsPbBr_3$ QDs have a large surface area and are capable of adsorbing more CO_2 on their surface.[32,43] As verified by the TEM analysis, the size of $CsPbBr_3$ QDs remained unchanged after forming a hybrid with Co_3O_4 HPs, indicating that it would exhibit similar CO_2 adsorption activity on its surface. Likewise, Co_3O_4 HPs also possess numerous adsorptions sites derived from their structural mesopores. Although most of the mesopores are occupied by $CsPbBr_3$ QDs (Fig. S11 and Table S2†), additional porosities are still accessible in the heterojunction (as shown in the green marked area in Fig. 1g and h). These porosities would actively endure the CO_2 adsorption.[52,57]

As the light absorption range is a key factor in solar-driven catalysis, to investigate the light-harvesting ability of the as-prepared components, diffuse reflectance spectra (DRS) were recorded. Both $CsPbBr_3$ QDs and Co_3O_4 HPs show a strong visible light response within the wavelength range of 400–600 nm, and their corresponding energy band gaps (E_g), determined to be 2.36 eV and 2.31 eV, respectively, are well-consistent with the literature (Fig. 4a and b and corresponding insets).[38,52] Where; E_g is estimated through Tauc plots using the equation $\alpha h\nu = A(h\nu - E_g)^n$ (see details in section 1.5 of the ESI†). It is to be noted that E_{1g} = 1.83 eV is attributed to the $O^{2-} \rightarrow Co^{3+}$ excitation and is not a real energy bandgap of Co_3O_4 HPs.[52,64–66] The enhanced light absorption ability of both components in the $CsPbBr_3$–Co_3O_4 heterojunction supports its higher catalytic activity. Moreover, the valence and conduction band positions (E_{VB} and E_{CB}) strongly define the thermodynamic feasibility of CO_2 reduction reactions. According to the reported results, the E_{CB} of Co_3O_4 and $CsPbBr_3$ are −0.64 eV [52] and −0.99 eV,[36] respectively, and correspondingly, the calculated E_{VB} for Co_3O_4 HPs and $CsPbBr_3$ QDs are 1.67 eV and 1.37 eV, respectively. Hence, the consequent $CsPbBr_3$–Co_3O_4 heterojunction possess efficient light harvesting ability with staggered band alignment as depicted in Fig. 5a, further endorsing an uninterrupted CO_2 conversion.

The rapid radiative recombination of photoinduced e^-–h^+ pairs in pristine $CsPbBr_3$ QDs can lead to low CO_2 conversion efficiency.[24] This was exclusively observed, where the intense photoluminescence (PL) spectra signal for pristine $CsPbBr_3$ (Fig. 4c) confirmed its low catalytic activity. However, after immobilizing $CsPbBr_3$ QDs on Co_3O_4 HPs, the results dramatically changed towards low PL intensity, identifying the significantly hindered recombination of e^-–h^+ pairs over the $CsPbBr_3$–Co_3O_4 heterojunction (Fig. 4c and Fig. S12†). This finding matched well with the enhanced photocatalytic performance. This also means, combining such photocatalysts can substantially quench the radiative recombination of the metal halide perovskite, thereby exhibiting high activity. Likewise, to investigate the charge transfer kinetics, PL decay was also inquired *via* time-resolved photoluminescence spectroscopy (TRPL, curves were fitted with a bi-exponential function, Table S3† and Fig. 4d). The $CsPbBr_3$–Co_3O_4 heterojunction demonstrated a shorter lifetime (τ_{avg} = 45.04 ns) in comparison with pristine $CsPbBr_3$ QDs (τ_{avg} = 47.43 ns). This outcome further verified the restrained recombination of e^-–h^+ pairs and their efficient separation in the $CsPbBr_3$–Co_3O_4 hybrid. Besides charge recombination, charge transfer kinetics and their directional transfer are decisive to realize an improved CO_2 conversion.[61,67,68] Therefore, these were investigated for the $CsPbBr_3$–Co_3O_4 heterojunction through electrochemical impedance spectroscopy (EIS) and transient photocurrent responses (TPR). The smallest arc radius was seen for the $CsPbBr_3$–Co_3O_4 heterojunction followed by $CsPbBr_3$ QDs

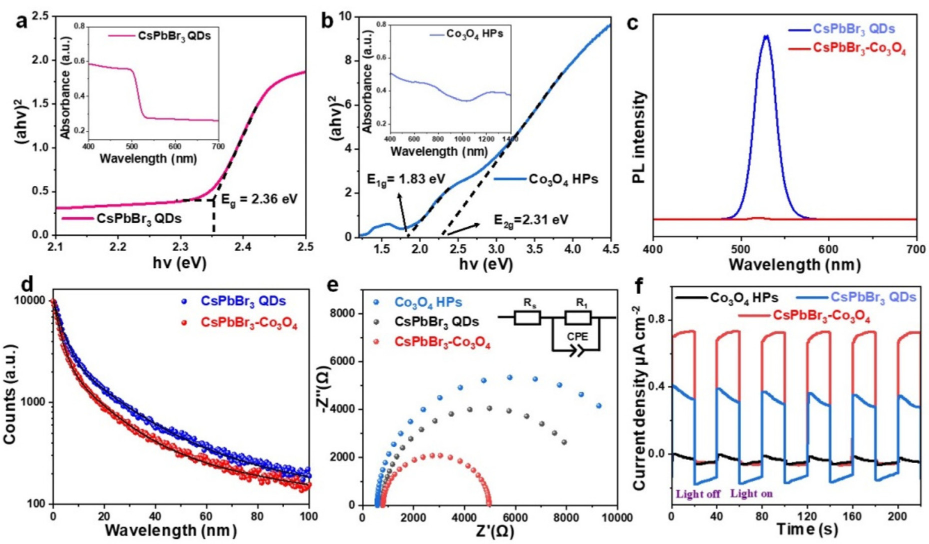

Fig. 4 Tauc plots for energy bands and their corresponding insets depicting the diffuse reflectance spectra curves for (a) $CsPbBr_3$ QDs and (b) Co_3O_4 HPs. (c) Steady-state photoluminescence spectra, and (d) time-resolved photoluminescence spectroscopy of $CsPbBr_3$ QDs and the $CsPbBr_3$–Co_3O_4 heterojunction. (e) Electrochemical impedance spectra and (f) transient photocurrent spectra of all the as-prepared products.

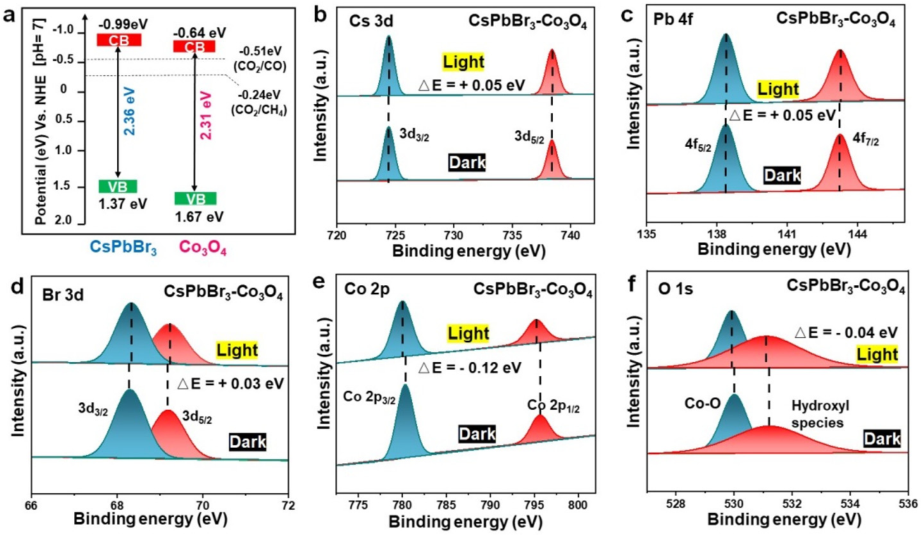

Fig. 5 (a) Redox potentials and band alignment of the $CsPbBr_3$–Co_3O_4 heterojunction. The *in situ* XPS analysis of (b) Cs 3d, (c) Pb 4f, (d) Br 3d, (e) Co 2p, and (f) O 1s, showing the electron-rich and electron-deficient sides in the $CsPbBr_3$–Co_3O_4 heterojunction.

and Co_3O_4 HPs (Fig. 4e). The markedly inhibited resistance in $CsPbBr_3$–Co_3O_4 would promote charge transfer. Likewise, the $CsPbBr_3$–Co_3O_4 shows the highest photocurrent with high repeatability (Fig. 4f). This result further supports the accelerated separation of e^-–h^+ pairs as well as highlights that an accessible route builds up (*i.e.*, heterointerface) by decorating $CsPbBr_3$ QDs on Co_3O_4 HPs.

3.4. Uncovering charge redistribution on the intimately coupled heterointerface and the corresponding catalytic mechanism

To further shed light on the interfacial charge-carrier flux, and their transfer route, particularly the accumulation of reductive electrons, the *in situ* XPS spectra were conducted under dark and visible light irradiation, respectively. As can be seen, the binding energies corresponding to Cs 3d, Pb 4f, and Br 3d exclusively underwent a positive shift (Fig. 5a–c) under light, which demonstrates a decrease of the electron density in the $CsPbBr_3$ side. In the meantime, the peak attributed to Co 2p and O 1s shifted to lower binding energy, suggesting an increased electron density at the Co_3O_4 side (Fig. 5e and f). Such patterns verify the continuous transfer of photoinduced electrons from $CsPbBr_3$ to Co_3O_4. In other words, Co_3O_4 plays a role as a supporting matrix to evoke and gather electrons from $CsPbBr_3$ QDs, allowing electron localization on the active surface of Co_3O_4. At the same time, an uninterrupted separation of e^-–h^+ pairs occurs in $CsPbBr_3$ owing to the significantly improved light harvesting ability and abundant exposed surface. Therefore, the electron-rich and electron-deficient phenomena occur simultaneously to balance the electron redistribution in the $CsPbBr_3$–Co_3O_4 heterojunction. Notably, except for the negative shift in O 1s spectra (Fig. 5f), no new peak belonging to OVs appeared, validating the structural permanence of Co_3O_4 in the heterojunction.

Furthermore, the work function (Φ) is another pivotal factor for charge carrier kinetics, particularly at the heterointerfaces. The Φ for $CsPbBr_3$ QDs and Co_3O_4 HPs are 4.39 eV and 5.74 eV respectively.[33,52] So, a larger Φ value of Co_3O_4 refers to its lower Fermi level (E_f) than that of $CsPbBr_3$, implying that the flow of electrons is from $CsPbBr_3$ to Co_3O_4 which is consistent with the outcomes of *in situ* XPS. This would hasten the extraction of reductive electrons from $CsPbBr_3$ to Co_3O_4, thus suppressing the recombination of e^-–h^+ pairs. In a word, $CsPbBr_3$ facilitated the rapid and continuous electron transfer *via* shorter diffusion pathways due to the size effect, and Co_3O_4 spontaneously accepted the electrons and accumulated on its active surface to exclusively participate in CO_2 reduction under the irradiation of solar light.

Based on the above results, the proposed CO_2 photoreduction mechanism over the $CsPbBr_3$–Co_3O_4 hybrid has been described. As illustrated in Fig. 6a, $CsPbBr_3$ and Co_3O_4 in the heterojunction have a staggered band alignment (type-II). In addition, the $CsPbBr_3$–Co_3O_4 heterojunction holds enough

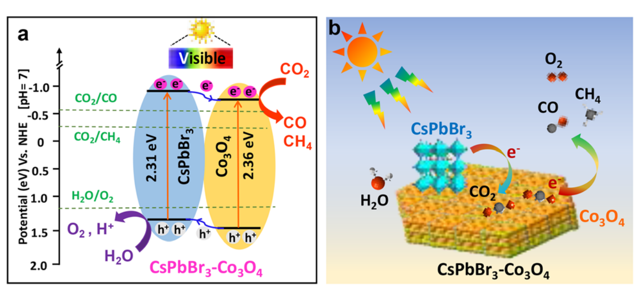

Fig. 6 (a) Photoexcited charge separation and their transfer route over the $CsPbBr_3$–Co_3O_4 heterojunction under visible light irradiation. (b) Schematic diagram depicting the continuous flow of electrons from $CsPbBr_3$ towards Co_3O_4 enabling the photocatalytic conversion of CO_2.

negative CB and positive VB potentials to reduce CO_2 and oxidize water, respectively. Under light irradiation, electrons and holes can be generated in both $CsPbBr_3$ and Co_3O_4. Subsequently, the photoinduced electrons are transferred from CB of $CsPbBr_3$ to CB of CO_3O_4 (Fig. 6b), causing electron localization at the CO_3O_4 side, making it suitable to conduct the CO_2 reduction reaction (as mentioned earlier in the *in situ* XPS analysis section). In the meantime, holes are transported in opposite directions *i.e.*, from VB of CO_3O_4 to VB of $CsPbBr_3$, building a hole-rich $CsPbBr_3$ side, favourable for oxidizing H_2O to O_2 and H^+. Accordingly, the breaking of C═O bonds in CO_2 occurred at the electron-rich Co_3O_4 side, where the coupling of electron and protons took place, for instance, $2e^-$ and $8e^-$ get coupled with $2H^+$ and $8H^+$ to produce CO and CH_4, respectively, as presented in eqn (1) and (2). Thus, the effective charge separation enables the uninterrupted electron–proton integrative reaction to realize highly efficient CO_2 photocatalytic reduction over the $CsPbBr_3$–Co_3O_4 heterojunction.

$$CO_2 + 2H^+ + 2e^- \rightarrow CO + H_2O \tag{1}$$

$$CO_2 + 8H^+ + 8e^- \rightarrow CH_4 + 2H_2O \tag{2}$$

4. Conclusions

In conclusion, a facile solution-processed room-temperature method was developed to fabricate a new $CsPbBr_3$–Co_3O_4 heterojunction photocatalyst for visible-light-driven CO_2 conversion. The successful formation of the $CsPbBr_3$–Co_3O_4 hybrid was confirmed by XRD, TEM, HRTEM and XPS analysis. The enhanced generation of CO (35.40 μmol g^{-1} h^{-1}) and CH_4 (29.2 μmol g^{-1} h^{-1}) with a high $R_{electron}$ rate (304.4 μmol g^{-1} h^{-1}) was realized on the $CsPbBr_3$–Co_3O_4 hybrid, which outperformed the counter products and some state-of-the-art photocatalysts. The formation of staggered band alignment and an intimately contacted heterointerface led to robust separation and directional transfer of charge carriers. Because of the uninterrupted flow of reductive e^-, an electron enrichment zone was obtained at the active site of Co_3O_4, which ensured the efficient conversion of CO_2. This work describes the potential of designing a new perovskite-based heterojunction that could enable efficient charge separation to achieve better solar-driven CO_2 conversion.

Author contributions

Xin Zhong: methodology, investigation, data curation, and writing the original draft. Xinmeng Liang: methodology, investigation, data curation, and writing the original draft. Xinyu Lin: methodology, investigation, and validation. Malik Zeeshan Shahid: writing the original draft, visualization, investigation, and data curation. Jin Wang: supervision, conceptualization, descriptions, and funding acquisition. Zhengquan Li: supervision, conceptualization, descriptions, and funding acquisition.

Conflicts of interest

There are no conflicts to declare.

Acknowledgements

This work was financially supported by the National Natural Science Foundation of China (21701143, 21975223), the Natural Science Foundation of Zhejiang Province (LGG19B010002, LZ22B030002), and the Industrial Key Projects of Jinhua City (2021A22383).

References

1 J. Wang, Y. Shi, Y. Wang and Z. Li, Rational design of metal halide perovskite nanocrystals for photocatalytic CO_2 reduction: Recent advances, challenges, and prospects, *ACS Energy Lett.*, 2022, **7**, 2043–2059.
2 S. Yin, X. Zhao, E. Jiang, Y. Yan, P. Zhou and P. Huo, Boosting water decomposition by sulfur vacancies for efficient CO_2 photoreduction, *Energy Environ. Sci.*, 2022, **15**, 1556–1562.
3 Y. Feng, C. Wang, P. Cui, C. Li, B. Zhang, L. Gan, S. Zhang, X. Zhang, X. Zhou, Z. Sun, K. Wang, Y. Duan, H. Li, K. Zhou, H. Huang, A. Li, C. Zhuang, L. Wang, Z. Zhang and X. Han, Ultrahigh photocatalytic CO_2 reduction efficiency and selectivity manipulation by single-tungsten-atom oxide at the atomic step of TiO_2, *Adv. Mater.*, 2022, **34**, 2109074.
4 J. Wang, L. Xiong, Y. Bai, Z. J. Chen, Q. Zheng, Y. Y. Shi, C. Zhang, G. C. Jiang and Z. Q. Li, Mn-doped perovskite nanocrystals for photocatalytic CO_2 reduction: Insight into the role of the charge carriers with prolonged lifetime, *Sol. RRL*, 2022, **6**, 2200294.
5 S. Xu, Q. Shen, J. Zheng, Z. Wang, X. Pan, N. Yang and G. Zhao, Advances in biomimetic photoelectrocatalytic reduction of carbon dioxide, *Adv. Sci.*, 2022, 2203941.
6 S. H. Teo, C. H. Ng, Y. H. Ng, A. Islam, S. Hayase and Y. H. Taufiq-Yap, Resolve deep-rooted challenges of halide perovskite for sustainable energy development and environmental remediation, *Nano Energy*, 2022, **99**, 107401.
7 E. Gong, S. Ali, C. B. Hiragond, H. S. Kim, N. S. Powar, D. Kim, H. Kim and S.-I. In, Solar fuels: research and development strategies to accelerate photocatalytic CO_2 conversion into hydrocarbon fuels, *Energy Environ. Sci.*, 2022, **15**, 880–937.
8 Y. Wang, E. Chen and J. Tang, Insight on reaction pathways of photocatalytic CO_2 conversion, *ACS Catal.*, 2022, **12**, 7300–7316.
9 Ž. Kovačič, B. Likozar and M. Huš, Photocatalytic CO_2 reduction: A review of Ab initio mechanism, kinetics, and multiscale modeling simulations, *ACS Catal.*, 2020, **10**, 14984–15007.

10 H. Bian, D. Li, S. Wang, J. Yan and S. F. Liu, 2D-C_3N_4 encapsulated perovskite nanocrystals for efficient photo-assisted thermocatalytic CO_2 reduction, *Chem. Sci.*, 2022, **13**, 1335–1341.
11 S. D. Yang, H. Y. Li, H. M. Li, H. M. Li, W. S. Qi, Q. Zhang, J. Zhu, P. Zhao and L. Chen, Rational design of 3D carbon nitrides assemblies with tunable nano-building blocks for efficient visible-light photocatalytic CO_2 conversion, *Appl. Catal., B*, 2022, **316**, 121612.
12 M. Gao, J. Zhang, P. Zhu, X. Liu and Z. Zheng, Unveiling the origin of alkali metal promotion in CO_2 methanation over Ru/ZrO_2, *Appl. Catal., B*, 2022, **314**, 121476.
13 L. Collado, P. Reñones, J. Fermoso, F. Fresno, L. Garrido, V. Pérez-Dieste, C. Escudero, M. D. Hernández-Alonso, J. M. Coronado, D. P. Serrano and V. A. D. O'Shea, The role of the surface acidic/basic centers and redox sites on TiO_2 in the photocatalytic CO_2 reduction, *Appl. Catal., B*, 2022, **303**, 120931.
14 S. Wei, Q. Heng, Y. Wu, W. Chen, X. Li and W. Shangguan, Improved photocatalytic CO_2 conversion efficiency on Ag loaded porous Ta_2O_5, *Appl. Surf. Sci.*, 2021, **563**, 150273.
15 X. Lin, S. Xia, L. Zhang, Y. Zhang, S. Sun, Y. Chen, S. Chen, B. Ding, J. Yu and J. Yan, Fabrication of flexible mesoporous black Nb_2O_5 nanofiber films for visible-light-driven photocatalytic CO_2 Reduction into CH_4, *Adv. Mater.*, 2022, **34**, 2200756.
16 J. Wang, S. Lin, N. Tian, T. Ma, Y. Zhang and H. Huang, Nanostructured metal sulfides: classification, modification strategy, and solar-driven CO_2 reduction application, *Adv. Funct. Mater.*, 2020, **31**, 2008008.
17 C. I. Ezugwu, S. Liu, C. Li, S. Zhuiykov, S. Roy and F. Verpoort, Engineering metal-organic frameworks for efficient photocatalytic conversion of CO_2 into solar fuels, *Coord. Chem. Rev.*, 2022, **450**, 214245.
18 C. B. Hiragond, N. S. Powar, J. Lee and S. I. In, Single-atom catalysts (SACs) for photocatalytic CO_2 reduction with H_2O: activity, product selectivity, stability, and surface chemistry, *Small*, 2022, **18**, 2201428.
19 X. J. Liu, T. Q. Chen, Y. H. Xue, J. C. Fan, S. L. Shen, M. S. A. A. Hossain, M. A. Amin, L. K. Pan, X. T. Xu and Y. Yamauchi, Nanoarchitectonics of MXene/semiconductor heterojunctions toward artificial photosynthesis via photocatalytic CO_2 reduction, *Coord. Chem. Rev.*, 2022, **459**, 214440.
20 S.-H. Wang, F. Khurshid, P.-Z. Chen, Y.-R. Lai, C.-W. Cai, P.-W. Chung, M. Hayashi, R.-J. Jeng, S.-P. Rwei and L. Wang, Solution-processable naphthalene diimide-based conjugated polymers as organocatalysts for photocatalytic CO_2 reaction with extremely stable catalytic activity for over 330 hours, *Chem. Mater.*, 2022, **34**, 4955–4963.
21 S. Chen, H. Yin, P. Liu, Y. Wang and H. Zhao, Stabilisation and performance enhancement strategies for halide perovskite photocatalysts, *Adv. Mater.*, 2022, **35**, 2203836.
22 H. Huang, D. Verhaeghe, B. Weng, B. Ghosh, H. Zhang, J. Hofkens, J. A. Steele and M. B. J. Roeffaers, Metal halide perovskite based heterojunction photocatalysts, *Angew. Chem., Int. Ed.*, 2022, **61**, e202203261.
23 S. Purohit, K. L. Yadav and S. Satapathi, Metal halide perovskite heterojunction for photocatalytic hydrogen generation: progress and future opportunities, *Adv. Mater. Interfaces*, 2022, **9**, 2200058.
24 L. Y. Wu, Y. F. Mu, X. X. Guo, W. Zhang, Z. M. Zhang, M. Zhang and T. B. Lu, Encapsulating perovskite quantum dots in iron-based metal-organic frameworks (MOFs) for efficient photocatalytic CO_2 reduction, *Angew. Chem., Int. Ed.*, 2019, **58**, 9491–9495.
25 X. Zhu, L. Ge, Y. Wang, M. Li, R. Zhang, M. Xu, Z. Zhao, W. Lv and R. Chen, Recent advances in enhancing and enriching the optical properties of Cl-based $CsPbX_3$ nanocrystals, *Adv. Opt. Mater.*, 2021, **9**, 2100058.
26 M. Ou, W. Tu, S. Yin, W. Xing, S. Wu, H. Wang, S. Wan, Q. Zhong and R. Xu, Amino–assisted anchoring of $CsPbBr_3$ perovskite quantum dots on porous g-C_3N_4 for enhanced photocatalytic CO_2 reduction, *Angew. Chem., Int. Ed.*, 2018, **57**, 13570–13574.
27 M. Madi, M. Tahir and S. Tasleem, Advances in structural modification of perovskite semiconductors for visible light assisted photocatalytic CO_2 reduction to renewable solar fuels: A review, *J. Environ. Chem. Eng.*, 2021, **9**, 106264.
28 Y. F. Mu, W. Zhang, X. X. Guo, G. X. Dong, M. Zhang and T. B. Lu, Water-tolerant lead halide perovskite nanocrystals as efficient photocatalysts for visible-light-driven CO_2 reduction in pure water, *ChemSusChem*, 2019, **12**, 4769–4774.
29 L. Clinckemalie, D. Valli, M. B. J. Roeffaers, J. Hofkens, B. Pradhan and E. Debroye, Challenges and opportunities for $CsPbBr_3$ perovskites in low- and high-energy radiation detection, *ACS Energy Lett.*, 2021, **6**, 1290–1314.
30 J. Wang, J. Liu, Z. Du and Z. Li, Recent advances in metal halide perovskite photocatalysts: Properties, synthesis and applications, *J. Energy Chem.*, 2021, **54**, 770–785.
31 G. Gao, Q. Xi, H. Zhou, Y. Zhao, C. Wu, L. Wang, P. Guo and J. Xu, Novel inorganic perovskite quantum dots for photocatalysis, *Nanoscale*, 2017, **9**, 12032–12038.
32 Q. A. Akkerman, T. P. T. Nguyen, S. C. Boehme, F. Montanarella, D. N. Dirin, P. Wechsler, F. Beiglbock, G. Raino, R. Erni, C. Katan, J. Even and M. V. Kovalenko, Controlling the nucleation and growth kinetics of lead halide perovskite quantum dots, *Science*, 2022, **377**, 1406–1412.
33 Z. Zhang, L. Li, Y. Jiang and J. Xu, Step-scheme photocatalyst of $CsPbBr_3$ quantum dots/BiOBr nanosheets for efficient CO_2 Photoreduction, *Inorg. Chem.*, 2022, **61**, 3351–3360.
34 X. Y. Yue, L. Cheng, J. J. Fan and Q. J. Xiang, 2D/2D $BiVO_4$/$CsPbBr_3$ S-scheme heterojunction for photocatalytic CO_2 reduction: Insights into structure regulation and Fermi level modulation, *Appl. Catal., B*, 2022, **304**, 120979.
35 C. C. Lin, T. R. Liu, S. R. Lin, K. M. Boopathi, C. H. Chiang, W. Y. Tzeng, W. C. Chien, H. S. Hsu, C. W. Luo, H. Y. Tsai, H. A. Chen, P. C. Kuo, J. Shiue, J. W. Chiou, W. F. Pong,

C. C. Chen and C. W. Chen, Spin-polarized photocatalytic CO_2 reduction of Mn-Doped perovskite nanoplates, *J. Am. Chem. Soc.*, 2022, **144**, 15718–15726.

36 Q. Wang, J. Wang, J. C. Wang, X. Hu, Y. Bai, X. Zhong and Z. Li, Coupling $CsPbBr_3$ quantum dots with covalent triazine frameworks for visible-light-driven CO_2 reduction, *ChemSusChem*, 2021, **14**, 1131–1139.

37 L. Ding, B. Borjigin, Y. Li, X. Yang, X. Wang and H. Li, Assembling an affinal 0D $CsPbBr_3$/2D $CsPb_2Br_5$ architecture by synchronously in situ growing $CsPbBr_3$ QDs and $CsPb_2Br_5$ nanosheets: enhanced activity and reusability for photocatalytic CO_2 reduction, *ACS Appl. Mater. Interfaces*, 2021, **13**, 51161–51173.

38 J. Wang, J. Wang, N. Li, X. Du, J. Ma, C. He and Z. Li, Direct Z-scheme 0D/2D heterojunction of $CsPbBr_3$ quantum Dots/Bi_2WO_6 nanosheets for efficient photocatalytic CO_2 reduction, *ACS Appl. Mater. Interfaces*, 2020, **12**, 31477–31485.

39 Y. Jiang, H. Y. Chen, J. Y. Li, J. F. Liao, H. H. Zhang, X. D. Wang and D. B. Kuang, Z-Scheme 2D/2D heterojunction of $CsPbBr_3$/Bi_2WO_6 for improved photocatalytic CO_2 reduction, *Adv. Funct. Mater.*, 2020, **30**, 2004293.

40 Z. J. Chen, Y. G. Hu, J. Wang, Q. Shen, Y. H. Zhang, C. Ding, Y. Bai, G. C. Jiang, Z. Q. Li and N. Gaponik, Boosting photocatalytic CO_2 reduction on $CsPbBr_3$ perovskite nanocrystals by immobilizing metal complexes, *Chem. Mater.*, 2020, **32**, 1517–1525.

41 S. Wan, M. Ou, Q. Zhong and X. Wang, Perovskite-type $CsPbBr_3$ quantum dots/UiO-66(NH_2) nanojunction as efficient visible-light-driven photocatalyst for CO_2 reduction, *Chem. Eng. J.*, 2019, **358**, 1287–1295.

42 Z.-C. Kong, J.-F. Liao, Y.-J. Dong, Y.-F. Xu, H.-Y. Chen, D.-B. Kuang and C.-Y. Su, Core@Shell $CsPbBr_3$@Zeolitic imidazolate framework nanocomposite for efficient photocatalytic CO_2 reduction, *ACS Energy Lett.*, 2018, **3**, 2656–2662.

43 Y. F. Xu, M. Z. Yang, B. X. Chen, X. D. Wang, H. Y. Chen, D. B. Kuang and C. Y. Su, A $CsPbBr_3$ perovskite quantum dot/Graphene oxide composite for photocatalytic CO_2 reduction, *J. Am. Chem. Soc.*, 2017, **139**, 5660–5663.

44 Q. Zhang, P. Yang, H. Zhang, J. Zhao, H. Shi, Y. Huang and H. Yang, Oxygen vacancies in Co_3O_4 promote CO_2 photoreduction, *Appl. Catal., B*, 2022, **300**, 120729.

45 Z. Feng, X. Zhu, J. Yang, K. Zhong, Z. Jiang, Q. Yu, Y. Song, Y. Hua, H. Li and H. Xu, Inherent facet-dominant effect for cobalt oxide nanosheets to enhance photocatalytic CO_2 reduction, *Appl. Surf. Sci.*, 2022, **578**, 151848.

46 P. Yang, Q. Zhang, Z. Yi, J. Wang and H. Yang, Rational electronic control of carbon dioxide reduction over cobalt oxide, *J. Catal.*, 2020, **387**, 119–128.

47 L. Huang, B. Li, B. Su, Z. Xiong, C. Zhang, Y. Hou, Z. Ding and S. Wang, Fabrication of hierarchical Co_3O_4@$CdIn_2S_4$ p–n heterojunction photocatalysts for improved CO_2 reduction with visible light, *J. Mater. Chem. A*, 2020, **8**, 7177–7183.

48 L. Wang, J. Wan, Y. Zhao, N. Yang and D. Wang, Hollow multi-shelled structures of Co_3O_4 dodecahedron with unique crystal orientation for enhanced photocatalytic CO_2 reduction, *J. Am. Chem. Soc.*, 2019, **141**, 2238–2241.

49 J. Y. Choi, C. K. Lim, B. Park, M. Kim, A. Jamal and H. Song, Surface activation of cobalt oxide nanoparticles for photocatalytic carbon dioxide reduction to methane, *J. Mater. Chem. A*, 2019, **7**, 15068–15072.

50 W. Chen, B. Han, C. Tian, X. Liu, S. Liang, H. Deng and Z. Lin, MOFs-derived ultrathin holey Co_3O_4 nanosheets for enhanced visible light CO_2 reduction, *Appl. Catal., B*, 2019, **244**, 996–1003.

51 X. Huang, Q. Shen, J. Liu, N. Yang and G. Zhao, A CO_2 adsorption-enhanced semiconductor/metal-complex hybrid photoelectrocatalytic interface for efficient formate production, *Energy Environ. Sci.*, 2016, **9**, 3161–3171.

52 C. Gao, Q. Meng, K. Zhao, H. Yin, D. Wang, J. Guo, S. Zhao, L. Chang, M. He, Q. Li, H. Zhao, X. Huang, Y. Gao and Z. Tang, Co_3O_4 Hexagonal platelets with controllable facets enabling highly efficient visible-light photocatalytic reduction of CO_2, *Adv. Mater.*, 2016, **28**, 6485–6490.

53 L. Wang, J. Deng, Z. Lou and T. Zhang, Nanoparticles-assembled Co_3O_4 nanorods p-type nanomaterials: One-pot synthesis and toluene-sensing properties, *Sens. Actuators, B*, 2014, **201**, 1–6.

54 L. Li, C. Zhang, R. Zhang, X. Gao, S. He, M. Liu, X. Li and W. Chen, 2D ultrathin Co_3O_4 nanosheet array deposited on 3D carbon foam for enhanced ethanol gas sensing application, *Sens. Actuators, B*, 2017, **244**, 664–672.

55 A. Aljabour, H. Coskun, D. H. Apaydin, F. Ozel, A. W. Hassel, P. Stadler, N. S. Sariciftci and M. Kus, Nanofibrous cobalt oxide for electrocatalysis of CO_2 reduction to carbon monoxide and formate in an acetonitrile-water electrolyte solution, *Appl. Catal., B*, 2018, **229**, 163–170.

56 Y. Gu, J. Ding, X. Tong, H. Yao, R. Yang and Q. Zhong, Photothermal catalyzed hydrogenation of carbon dioxide over porous nanosheet Co_3O_4, *J. CO_2 Util.*, 2022, **61**, 102003.

57 X. Zhu, H. Ji, J. Yi, J. Yang, X. She, P. Ding, L. Li, J. Deng, J. Qian, H. Xu and H. Li, A specifically exposed cobalt oxide/carbon nitride 2D heterostructure for carbon dioxide photoreduction, *Ind. Eng. Chem. Res.*, 2018, **57**, 17394–17400.

58 W. Yang, G. Ma, Y. Fu, K. Peng, H. Yang, X. Zhan, W. Yang, L. Wang and H. Hou, Rationally designed Ti_3C_2 MXene@TiO_2/$CuInS_2$ Schottky/S-scheme integrated heterojunction for enhanced photocatalytic hydrogen evolution, *Chem. Eng. J.*, 2022, **429**, 132381.

59 X.-T. Liu, B.-H. Li, X.-J. Wang, Y.-L. Li, J. Zhao, Y.-P. Li and F.-T. Li, Enhanced schottky effect in the Ni_2P cocatalyst via work function up-shift induced by MoO_2 for boosting photocatalytic hydrogen evolution, *ACS Sustainable Chem. Eng.*, 2022, **10**, 10627–10640.

60 K. Liu, H. Zhang, T. Fu, L. Wang, R. Tang, Z. Tong and X. Huang, Construction of BiOBr/Ti_3C_2/exfoliated montmorillonite Schottky junction: New insights into exfoliated montmorillonite for inducing MXene oxygen functionali-

zation and enhancing photocatalytic activity, *Chem. Eng. J.*, 2022, **438**, 135609.

61 Y. Li, Q. Zhao, Y. Zhang, Y. Li, L. Fan, F.-T. Li and X. Li, In-situ construction of sequential heterostructured CoS/CdS/CuS for building "electron-welcome zone" to enhance solar-to-hydrogen conversion, *Appl. Catal., B*, 2022, **300**, 120763.

62 J. Li, L. Xu, T. Wang, J. Song, J. Chen, J. Xue, Y. Dong, B. Cai, Q. Shan, B. Han and H. Zeng, 50-Fold EQE Improvement up to 6.27% of solution-processed all-inorganic perovskite $CsPbBr_3$ QLEDs via surface ligand density control, *Adv. Mater.*, 2017, **29**, 1603885.

63 N. Li, X. Chen, J. Wang, X. Liang, L. Ma, X. Jing, D. L. Chen and Z. Li, ZnSe Nanorods-$CsSnCl_3$ perovskite heterojunction composite for photocatalytic CO_2 reduction, *ACS Nano*, 2022, **16**, 3332–3340.

64 D. Barreca, C. Massignan, S. Daolio, M. Fabrizio, C. Piccirillo, L. Armelao and E. Tondello, Composition and microstructure of cobalt oxide thin films obtained from a novel cobalt(II) precursor by chemical vapor deposition, *Chem. Mater.*, 2001, **13**, 588–593.

65 Z. Hu, L. Hao, F. Quan and R. Guo, Recent developments of Co_3O_4-based materials as catalysts for the oxygen evolution reaction, *Catal. Sci. Technol.*, 2022, **12**, 436–461.

66 Y. Xu, F. Zhang, T. Sheng, T. Ye, D. Yi, Y. Yang, S. Liu, X. Wang and J. Yao, Clarifying the controversial catalytic active sites of Co_3O_4 for the oxygen evolution reaction, *J. Mater. Chem. A*, 2019, **7**, 23191–23198.

67 W. He, L. Liu, T. Ma, H. Han, J. Zhu, Y. Liu, Z. Fang, Z. Yang and K. Guo, Controllable morphology $CoFe_2O_4$/g-C_3N_4 p-n heterojunction photocatalysts with built-in electric field enhance photocatalytic performance, *Appl. Catal., B*, 2022, **306**, 121107.

68 S. Bai, J. Jiang, Q. Zhang and Y. Xiong, Steering charge kinetics in photocatalysis: intersection of materials syntheses, characterization techniques and theoretical simulations, *Chem. Soc. Rev.*, 2015, **44**, 2893–2939.